

Research Article

Design and Steady-State Performance of a Novel Winding Type Permanent Magnet Coupling with Slip Power Recovery Function

Lei Xia and Haobin Jiang

School of Automotive and Traffic Engineering, Jiangsu University, Zhenjiang 212013, China

Correspondence should be addressed to Haobin Jiang; jianghb@ujs.edu.cn

Received 24 February 2017; Accepted 11 May 2017; Published 30 May 2017

Academic Editor: Dane Quinn

Copyright © 2017 Lei Xia and Haobin Jiang. This is an open access article distributed under the Creative Commons Attribution License, which permits unrestricted use, distribution, and reproduction in any medium, provided the original work is properly cited.

A novel winding type permanent magnet coupling (WTPMC) is proposed to work as an adjustable speed drive with slip power recovery function. As a kind of dual-mechanical-port electric machine with radial-flux configuration, the WTPMC consists of an outer rotor embedded with three-phase windings, an inner rotor populated with permanent magnets, and a slip power recovery circuit comprising a rectifier, a boost converter, and an ultracapacitor. The working principle of the WTPMC is presented, and its mathematical model is derived. To develop a WTPMC prototype for automotive applications, two-dimensional (2D) finite element analysis (FEA) is conducted using Ansoft Maxwell software to study the steady-state (constant slip speed) performance. For the experimental validation, the WTPMC prototype is manufactured and tested on a test bench. To show the accuracy of the 2D FEA, the computed results are compared with those obtained from experimental measurements. It is shown that the agreement between the 2D FEA and experimental results is good. Moreover, the WTPMC prototype can operate in the output speed range under different load torque conditions. The slip power recovery efficiency for the 2D FEA is 66.7%, while, for experimental measurements, it is 57.2%.

1. Introduction

Magnetic couplings have been widely employed in various industrial applications that require power transmission with no mechanical connection. They can transmit torque through an air gap between two rotors that are, respectively, attached to the prime mover and the load. There are mainly three types of magnetic couplings, namely, electromagnetic coupling [1, 2], permanent magnet synchronous coupling [3–9], and permanent magnet eddy current coupling [10–16]. These types of magnetic couplings have both axial-flux or radial-flux configurations.

The electromagnetic coupling and permanent magnet eddy current coupling can be used as adjustable speed drives, since their torque generation is based on the relative motion between one rotor generating a magnetic field and another rotor acting as a conductive part. By now, some corporations, like MagnaDrive, Frings Auerbach, and Sandvik, have developed related products and put them into the market. However, these couplings have their own disadvantages. For

electromagnetic couplings, the magnetic field is created using a winding system and can be regulated by varying the exciting current. The disadvantage lies in that it requires an electrical supply system and consumes considerable energy during operation. For permanent magnet eddy current couplings, the magnetic field is produced by permanent magnets, thus eliminating the electrical supply system. In this case, the magnetic field can be regulated by varying the air gap length for axial-flux configuration or by adjusting the overlapping area between two rotors for radial-flux configuration. Nevertheless, in practical applications, it becomes difficult for mostly used axial-flux couplings to realize the millimeter-level precision of air gap adjustment via a mechanism. Moreover, due to the induction of eddy current in the conductive rotor, the slip power, that is the power difference between input and output terminals, is dissipated as heat and can not be recovered. This will significantly decrease the coupling's efficiency under large-slip conditions. Therefore, the normal working range of permanent magnet eddy current couplings corresponds to low slip values. Note that it is promising to

develop a type of magnetic coupling which can also work efficiently under large-slip conditions, and one of the feasible ways is trying to recover the slip power.

The design and analysis of magnetic couplings can be achieved with the numerical or analytical methods. Numerical approaches, such as finite element analysis (FEA), can give accurate results considering the material nonlinearity and geometric details [17]. However, magnetic coupling is an inherent three-dimensional (3D) geometry from the modeling point of view, which takes long computation time for FEA. In order to simplify the analysis, the 3D problem can be reduced to a two-dimensional (2D) one by introducing a cutting plane for creating the cross section. Note that it becomes necessary to verify the accuracy of the 2D FEA by comparing with experimental or analytical approaches.

Inspired by the above discussion, this paper proposes a novel winding type permanent magnet coupling (WTPMC), which can work as an adjustable speed drive with slip power recovery function. The structure and working principle of the WTPMC are presented. Based on the working principle, its mathematical model is derived. In order to develop a WTPMC prototype for automotive applications, the 2D FEA is conducted using Ansoft Maxwell software to study the steady-state (constant slip speed) performance. For the experimental validation, the WTPMC prototype is manufactured and tested on a test bench. The results computed with the 2D FEA are compared with those obtained from experimental measurements.

2. Design of WTPMC

The schematic of the proposed WTPMC is illustrated in Figure 1. It is basically composed of three components: (1) an outer rotor that is embedded with three-phase windings and attached to the input shaft; (2) an inner rotor that is populated with permanent magnets and attached to the output shaft; (3) a slip power recovery circuit comprising a diode bridge rectifier, a boost converter based on insulated gate bipolar transistor (IGBT), an ultracapacitor, and an electronic control unit (ECU). Note that the outer and inner rotors are usually called the rotor assembly. Moreover, the three-phase windings are connected to the slip power recovery circuit via slip rings. The permanent magnets are radially magnetized, as indicated by arrows on them. In general, the WTPMC can be regarded as a kind of dual-mechanical-port electric machine with radial-flux configuration.

The working principle of the WTPMC is as follows. When the prime mover drives the input shaft and outer rotor to rotate, the relative motion between outer and inner rotors induces alternating current (AC) in the three-phase windings under the excitation of magnetic field produced by permanent magnets. The induced AC then interacts with the magnetic field to produce an electromagnetic torque against the load, which drives the inner rotor to rotate at a speed lower than the outer rotor speed. Note that the inner rotor speed is regarded as the output speed of the WTPMC. Moreover, the induced AC is transformed into direct current (DC) through the rectifier, and the boost converter is assumed to operate in continuous conduction

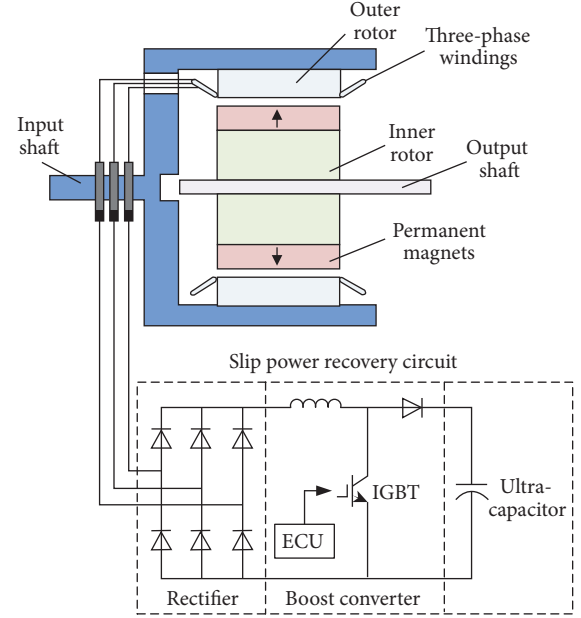


FIGURE 1: Schematic of WTPMC.

mode (CCM). In order to work as an adjustable speed drive, the ECU regulates the duty cycle of the IGBT to change the DC in the circuit, so as to further control the electromagnetic torque and output speed of the WTPMC. In addition, in order to achieve slip power recovery function, the DC charges the ultracapacitor when the IGBT is turned OFF during the operation of the boost converter.

3. Mathematical Modeling

Based on the working principle, the mathematical model of the WTPMC is derived.

The equivalent circuits of slip power recovery when the IGBT is turned ON or OFF are shown in Figure 2, respectively. The parameters are as follows: U represents the effective back-electromotive force (EMF); i denotes the circuit current; L_w and R_w are the equivalent inductance and resistance of the three-phase windings, respectively; L_{bc} denotes the inductance of the boost converter's inductor; U_c represents the terminal voltage of the ultracapacitor.

The effective back-EMF is proportional to the slip speed Ω that is the speed difference between outer and inner rotors, which can be expressed as

$$U = k_e \Omega = k_e (\Omega_1 - \Omega_2), \quad (1)$$

where k_e is the back-EMF coefficient. Ω_1 and Ω_2 denote the outer rotor speed and inner rotor speed, respectively.

(i) When the IGBT is turned ON, the circuit relations meet the following equations:

$$\begin{aligned} U &= (L_w + L_{bc}) \dot{i} + R_w i, \\ C \dot{U}_c &= 0. \end{aligned} \quad (2)$$

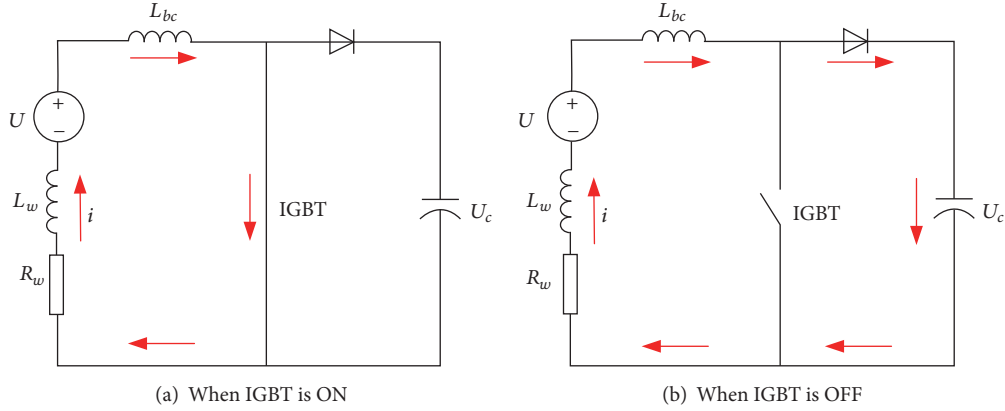


FIGURE 2: Equivalent circuit of slip power recovery.

(ii) When the IGBT is turned OFF, we can get

$$\begin{aligned} U &= (L_w + L_{bc})\dot{i} + R_w i + U_c, \\ C\dot{U}_c &= i, \end{aligned} \quad (3)$$

where C is the rated capacity of the ultracapacitor.

Combining (2)-(3) and using the averaging method, we have

$$\begin{aligned} U &= (L_w + L_{bc})\dot{i} + R_w i + (1 - D)U_c, \\ C\dot{U}_c &= (1 - D)i, \end{aligned} \quad (4)$$

where D is the duty cycle of the IGBT.

Moreover, the electromagnetic torque T_e is proportional to the circuit current, which can be written as

$$T_e = k_T i, \quad (5)$$

where k_T denotes the electromagnetic torque coefficient.

The motion equations for outer and inner rotors are given by

$$\begin{aligned} J_1 \dot{\Omega}_1 + B_1 \Omega_1 &= T_{pm} - T_e, \\ J_2 \dot{\Omega}_2 + B_2 \Omega_2 &= T_e - T_l, \end{aligned} \quad (6)$$

where J_1 and B_1 are the moment of inertia and viscous damping coefficient of the outer rotor, respectively. J_2 and B_2 are the moment of inertia and viscous damping coefficient of the inner rotor, respectively. T_{pm} denotes the prime mover torque, and T_l represents the load torque.

In addition, the power recovered by the ultracapacitor P can be obtained as

$$P = \frac{C(U_{c2}^2 - U_{c1}^2)}{2\Delta t}, \quad (7)$$

where U_{c1} and U_{c2} represent the initial and final terminal voltage of the ultracapacitor, respectively. Δt denotes the time duration.

TABLE 1: Design requirements.

| Parameter | Value |
|---------------------------------|---------|
| Outer rotor speed (r/min) | 500 |
| Inner rotor speed range (r/min) | 100–400 |
| Maximum load torque (N·m) | 40 |
| Maximum input power (kW) | 2.094 |
| Maximum output power (kW) | 1.675 |

4. FEA Approach

To develop a WTPMC prototype for automotive applications, its 2D FEA is conducted using Ansoft Maxwell software.

Table 1 gives the design requirements for the WTPMC prototype. Note that the outer rotor speed is 500 r/min and the inner rotor speed range is 100–400 r/min, which means that the maximum slip speed is 400 r/min that corresponds to a slip rate of 80%. Under the steady-state condition, the constant slip speed corresponds to constant inner rotor speed, which means that the electromagnetic torque nearly equals the load torque. Table 1 shows that the maximum load torque is 40 N·m. In this case, the maximum input power is 2.094 kW, and the maximum output power can be up to 1.675 kW with the inner rotor speed to be 400 r/min.

According to the above design requirements, a 2D geometrical model is established, as shown in Figure 3. Table 2 lists its main geometrical and physical parameters. These parameters have been optimized, but the optimization procedure is not discussed in this paper. As can be seen in Figure 3, the geometrical model shows the cross section of the rotor assembly normal to the axial direction. The double layer three-phase windings are housed inside 18 slots. Moreover, there are 8 pole-pairs of permanent magnets alternating in the direction of magnetization, as indicated by arrows on them. To simulate the slip power recovery circuit, an equivalent circuit model is built in the module of Maxwell Circuit Editor, as shown in Figure 4.

Based on the geometrical model, the adaptive meshing technique is adopted to obtain a 2D finite element (FE) model, as shown in Figure 5. The meshing size of outer and

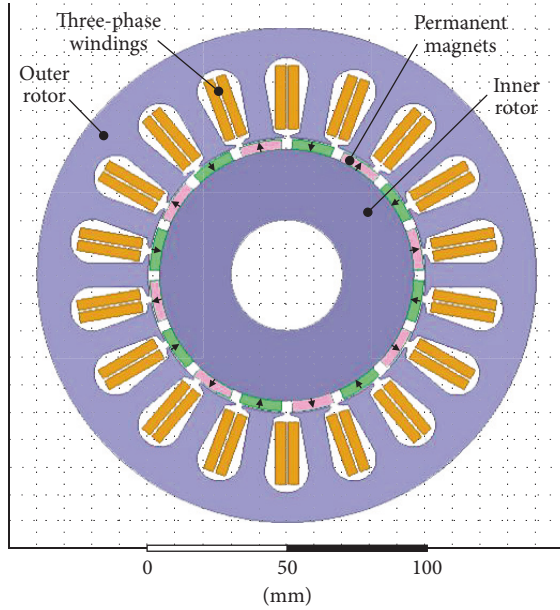


FIGURE 3: 2D geometrical model.

TABLE 2: Geometrical and physical parameters.

| Parameter | Value |
|----------------------------------|-------|
| Outer radius of outer rotor (mm) | 90 |
| Inner radius of outer rotor (mm) | 50 |
| Inner radius of inner rotor (mm) | 20 |
| Axial length of rotors (mm) | 100 |
| Air gap length (mm) | 1.5 |
| Permanent magnets thickness (mm) | 6 |
| Slots number | 18 |
| Pole-pairs number | 8 |

inner rotors, three-phase windings, and permanent magnets are 8.1 mm, 6.3 mm, and 1.8 mm, respectively. The FEA can be conducted after the preprocessing steps are done.

5. Experimental Approach

For the experimental validation, the WTPMC prototype is manufactured by a local corporation which specializes in permanent magnetic equipment. Figures 6 and 7 show the rotor assembly with casting and the slip power recovery circuit, respectively. According to the corporation's request, the rotor assembly without casting is not shown in this paper. Moreover, as can be seen from the bottom of Figure 7, an ultracapacitor produced by the corporation of Maxwell Technologies is used for slip power recovery with the rated capacity of 165 F and rated voltage of 48 V.

The steady-state and dynamic performance of the WTPMC prototype is tested on a test bench, whose schematic and photograph are shown in Figures 8 and 9, respectively. In addition to the WTPMC prototype, the test bench mainly consists of a three-phase induction motor, a dynamometer,

TABLE 3: Comparison of effective back-EMF.

| Slip speed (r/min) | Effective back-EMF (V) | |
|--------------------|------------------------|--------------|
| | 2D FEA | Experimental |
| 0 | 0 | 2 |
| 100 | 8.6 | 8 |
| 200 | 17.2 | 16.3 |
| 300 | 25.6 | 24.4 |
| 400 | 34.2 | 32.5 |
| 500 | 42.8 | 40.8 |

two torque/speed sensors, and a control cabinet. The three-phase induction motor acts as the prime mover, and the dynamometer applies the load torque. One torque/speed sensor is set between the three-phase induction motor and the WTPMC prototype for measuring the outer rotor speed. Moreover, another torque/speed sensor is set between the WTPMC prototype and the dynamometer for measuring the inner rotor speed. The control cabinet is used to monitor and adjust the signals such as the load torque, the terminal voltage of the ultracapacitor, and the duty cycle of the IGBT.

6. Results and Discussion

In this section, we use the 2D FEA to study the steady-state (constant slip speed) performance of the developed WTPMC prototype. In order to verify the effectiveness of the 2D FEA, the computed results are compared with those obtained from experimental measurements.

6.1. Effective Back-EMF versus Slip Speed. Figure 10 shows the effective back-EMF versus the slip speed for the WTPMC prototype. Table 3 gives the comparison of effective back-EMF. Good agreements can be observed between the 2D FEA and experimental results. It can be seen that the deviations of effective back-EMF between the 2D FEA and experimental results for each slip speed are always below 10%, except for the case of zero slip speed. Due to the remanent flux density of permanent magnets in experiments, there exists an effective back-EMF of 2 V for zero slip speed. Nevertheless, the remanent flux density of permanent magnets is not considered in the 2D FEA. Moreover, the 2D FEA and experimental results indicate the proportional relationship between effective back-EMF and slip speed, as previously described in (1). According to Table 3 and (1), the back-EMF coefficient k_e is approximated to be 0.086 and 0.081 for the 2D FEA and experimental results, respectively.

6.2. Electromagnetic Torque versus Circuit Current. Figure 11 shows the electromagnetic torque versus the circuit current for the WTPMC prototype. Table 4 gives the comparison of circuit current. Once again, the agreement between the 2D FEA and experimental results is good. It can be observed that the deviations of circuit current between the 2D FEA and experimental results for each electromagnetic torque are always below 10%. Moreover, the 2D FEA and experimental

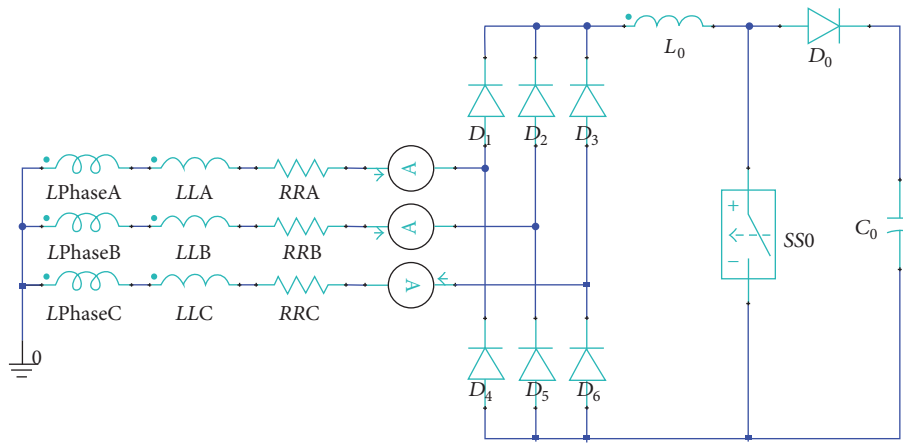


FIGURE 4: Equivalent circuit model.

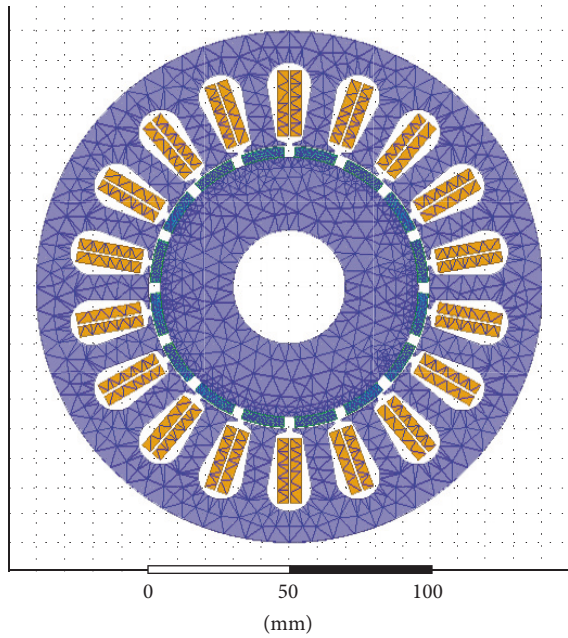


FIGURE 5: 2D FE model.



FIGURE 7: Slip power recovery circuit.



FIGURE 6: Rotor assembly with casting.

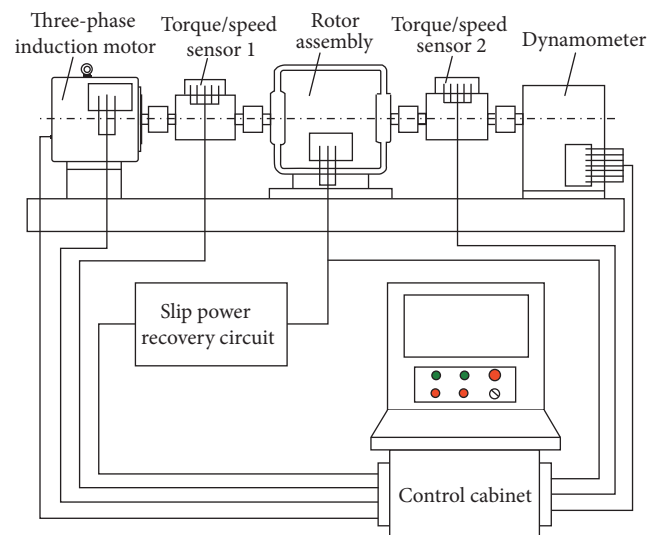


FIGURE 8: Schematic of test bench.



A: three-phase induction motor
 B: torque/speed sensor 1
 C: rotor assembly
 D: torque/speed sensor 2
 E: dynamometer
 F: slip power recovery circuit
 G: control cabinet

FIGURE 9: Photograph of test bench.

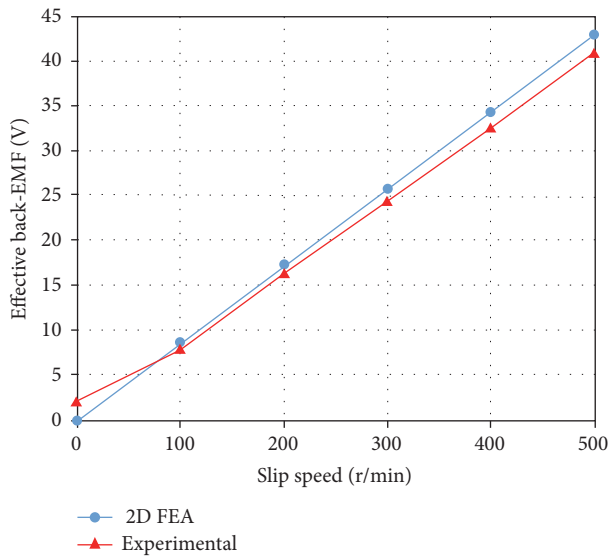


FIGURE 10: Effective back-EMF versus slip speed.

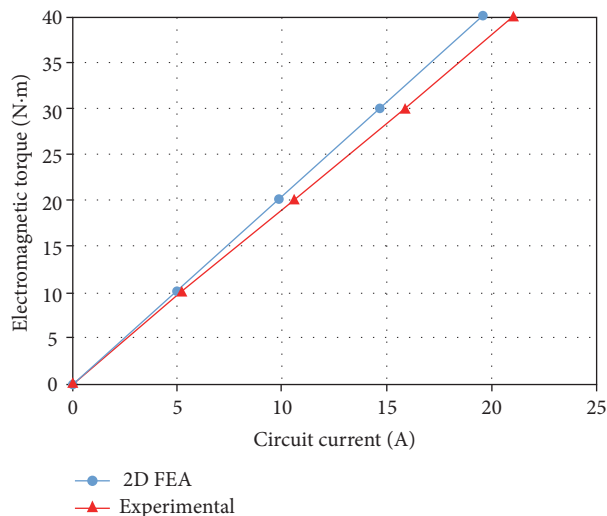


FIGURE 11: Electromagnetic torque versus circuit current.

TABLE 4: Comparison of circuit current.

| Electromagnetic torque (N·m) | Circuit current (A) | |
|------------------------------|---------------------|--------------|
| | 2D FEA | Experimental |
| 0 | 0 | 0 |
| 10 | 5 | 5.2 |
| 20 | 9.9 | 10.6 |
| 30 | 14.7 | 15.9 |
| 40 | 19.6 | 21.1 |

TABLE 5: Duty cycle of IGBT with different output speed and load torque (2D FEA).

| Duty cycle of IGBT | Load torque (N·m) | | | |
|--------------------|-------------------|------|------|------|
| | 10 | 20 | 30 | 40 |
| 100 | 0.25 | 0.29 | 0.32 | 0.36 |
| 200 | 0.45 | 0.49 | 0.52 | 0.56 |
| 300 | 0.64 | 0.68 | 0.72 | 0.76 |
| 400 | 0.84 | 0.88 | 0.92 | 0.96 |

TABLE 6: Duty cycle of IGBT with different output speed and load torque (experimental).

| Duty cycle of IGBT | Load torque (N·m) | | | |
|--------------------|-------------------|------|------|------|
| | 10 | 20 | 30 | 40 |
| 100 | 0.29 | 0.33 | 0.37 | 0.42 |
| 200 | 0.47 | 0.52 | 0.56 | 0.6 |
| 300 | 0.66 | 0.71 | 0.75 | 0.79 |
| 400 | 0.86 | 0.9 | 0.94 | 0.99 |

results indicate that the electromagnetic torque has a proportional relationship with regard to the circuit current, as previously expressed in (5). According to Table 4 and (5), the electromagnetic torque coefficient k_T is approximated to be 2.02 and 1.89 for the 2D FEA and experimental results, respectively.

6.3. Performance as Adjustable Speed Drive. As an adjustable speed drive, the WTPMC prototype should have the ability to operate in the output speed range. Tables 5 and 6 give the duty cycle of the IGBT with different output speed and load torque for the 2D FEA and experimental measurements, respectively. In this case, the terminal voltage of the ultra-capacitor is 43 V. For ease of comparison between the 2D FEA and experimental results, the output speed versus the duty cycle of the IGBT for the load torque of 10 N·m, 20 N·m, 30 N·m, and 40 N·m is shown in Figures 12–15, respectively. Since the deviations of the duty cycle of the IGBT for each output speed are always below 20%, the agreement between the 2D FEA and experimental results is good. It is shown that the WTPMC prototype can operate in the output speed range under different load torque conditions. With the same load torque, the duty cycle of the IGBT increases linearly with the increase of output speed. Moreover, with the same output speed, the duty cycle of the IGBT increases linearly with the increase of load torque.

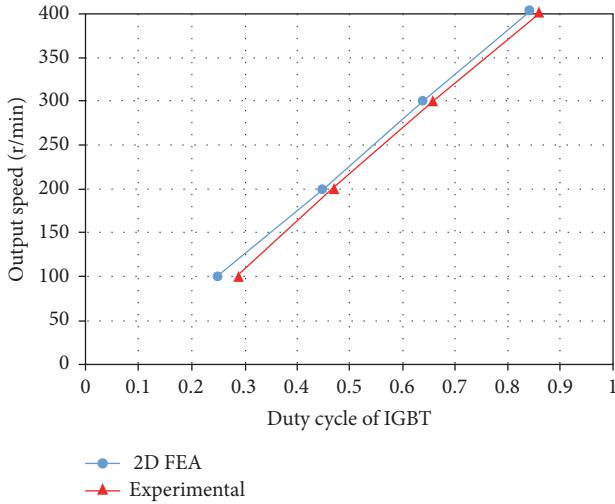


FIGURE 12: Output speed versus duty cycle of IGBT for load torque of 10 N·m.

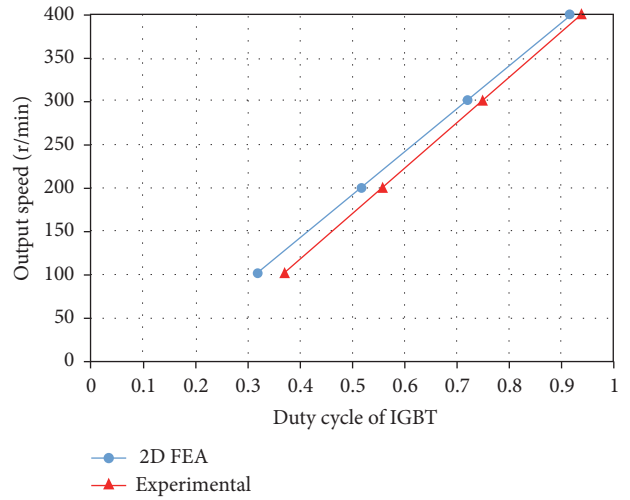


FIGURE 14: Output speed versus duty cycle of IGBT for load torque of 30 N·m.

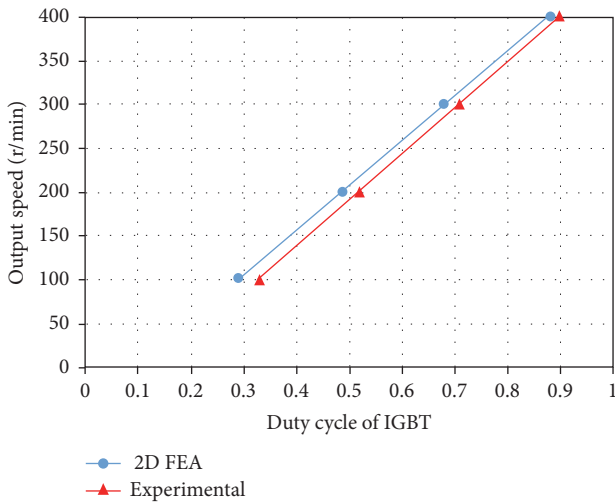


FIGURE 13: Output speed versus duty cycle of IGBT for load torque of 20 N·m.

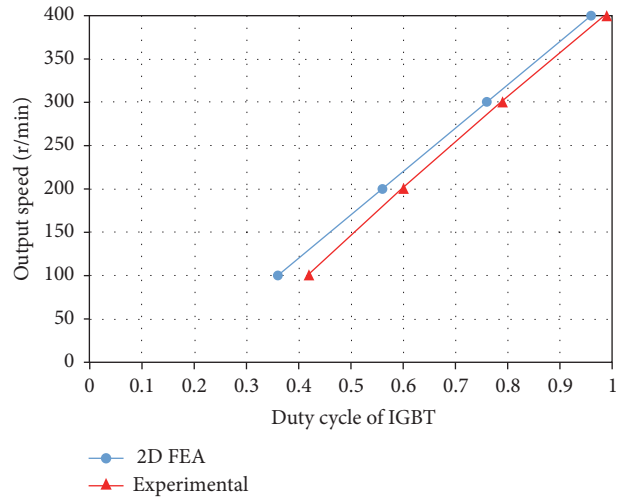


FIGURE 15: Output speed versus duty cycle of IGBT for load torque of 40 N·m.

TABLE 7: Comparison of performance indices.

| Performance indices | 2D FEA | Experimental |
|--|---------|--------------|
| Final terminal voltage of ultracapacitor (V) | 43.78 | 43.67 |
| Power recovered by ultracapacitor (W) | 1116.86 | 958.17 |
| Slip power recovery efficiency (%) | 66.7 | 57.2 |

6.4. Slip Power Recovery Performance. The slip power recovery efficiency, which is the ratio of the power recovered by the ultracapacitor to the slip power, is selected as the crucial index to evaluate the slip power recovery performance. Figure 16 demonstrates the response of the terminal voltage of the ultracapacitor, and Table 7 gives the comparison of performance indices. In this case, the slip speed is constant at 400 r/min for the load torque of 40 N·m, which corresponds to the maximum slip power of 1675 W. From Figure 16,

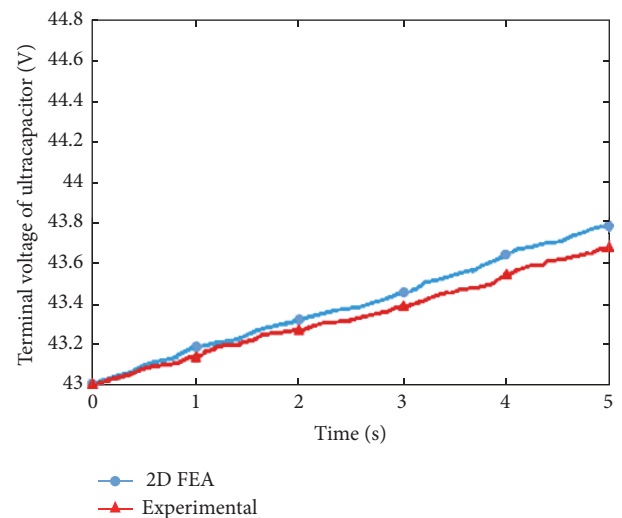


FIGURE 16: Terminal voltage of ultracapacitor.

good agreements can be observed between the 2D FEA and experimental results. Note that the initial terminal voltage of the ultracapacitor is 43 V, and the time duration is 5 s. The final terminal voltages of the ultracapacitor for the 2D FEA and experimental measurements are 43.78 V and 43.67 V, respectively. According to (7), the power recovered by the ultracapacitor can be calculated, as shown in Table 7. Furthermore, the slip power recovery efficiency is calculated to be 66.7% and 57.2% for the 2D FEA and experimental measurements, respectively.

7. Conclusions

In this paper, a novel WTPMC has been proposed to work as an adjustable speed drive with slip power recovery function. The structure and working principle of the WTPMC have been presented. Based on the working principle, its mathematical model has been derived. In order to develop a WTPMC prototype for automotive applications, the 2D FEA has been conducted using Ansoft Maxwell software to study the steady-state (constant slip speed) performance. For the experimental validation, the WTPMC prototype has been manufactured and tested on a test bench. The results computed with the 2D FEA have been compared with those obtained from experimental measurements. It is shown that the agreement between the 2D FEA and experimental results is good. Moreover, the WTPMC prototype can operate in the output speed range under different load torque conditions. The slip power recovery efficiency for the 2D FEA is 66.7%, while, for experimental measurements, it is 57.2%.

Conflicts of Interest

The authors declare that there are no conflicts of interest regarding the publication of this paper.

Acknowledgments

This work was funded by the National Natural Science Foundation of China (no. 51275211) and the Special Fund of Jiangsu Province for the Transformation of Scientific and Technological Achievements (no. BR2015168). The authors wish to acknowledge Jiangsu Magnet Valley Technologies Co., Ltd., for manufacturing the WTPMC prototype.

References

- [1] R. You, B. Barahona, J. Chai, and N. A. Cutululis, "A novel wind turbine concept based on an electromagnetic coupler and the study of its fault ride-through capability," *Energies*, vol. 6, no. 11, pp. 6120–6136, 2013.
- [2] B. Tang, H.-B. Jiang, Z. Xu, G.-Q. Geng, and X. Xu, "Dynamics of electromagnetic slip coupling for hydraulic power steering application and its energy-saving characteristics," *Journal of Central South University*, vol. 22, no. 5, article no. 2720, pp. 1994–2000, 2015.
- [3] R. Ravaut, G. Lemarquand, V. Lemarquand, and C. Depollier, "Permanent magnet couplings: Field and torque three-dimensional expressions based on the coulombian model," *IEEE Transactions on Magnetics*, vol. 45, no. 4, pp. 1950–1958, 2009.
- [4] R. Ravaut, V. Lemarquand, and G. Lemarquand, "Analytical design of permanent magnet radial couplings," *IEEE Transactions on Magnetics*, vol. 46, no. 11, pp. 3860–3865, 2010.
- [5] T. Lubin, S. Mezani, and A. Rezzoug, "Simple analytical expressions for the force and torque of axial magnetic couplings," *IEEE Transactions on Energy Conversion*, vol. 27, no. 2, pp. 536–546, 2012.
- [6] T. Lubin, S. Mezani, and A. Rezzoug, "Experimental and theoretical analyses of axial magnetic coupling under steady-state and transient operations," *IEEE Transactions on Industrial Electronics*, vol. 61, no. 8, pp. 4356–4365, 2014.
- [7] B. Dolisy, S. Mezani, T. Lubin, and J. Leveque, "A New Analytical Torque Formula for Axial Field Permanent Magnets Coupling," *IEEE Transactions on Energy Conversion*, vol. 30, no. 3, pp. 892–899, 2015.
- [8] H.-B. Kang and J.-Y. Choi, "Parametric analysis and experimental testing of radial flux type synchronous permanent magnet coupling based on analytical torque calculations," *Journal of Electrical Engineering and Technology*, vol. 9, no. 3, pp. 926–931, 2014.
- [9] S. Hogberg, B. B. Jensen, and F. B. Bendixen, "Design and demonstration of a test-rig for static performance-studies of permanent magnet couplings," *IEEE Transactions on Magnetics*, vol. 49, no. 12, pp. 5664–5670, 2013.
- [10] A. S. El-Wakeel, "Design optimization of PM couplings using hybrid particle swarm optimization-simplex method (PSO-SM) algorithm," *Electric Power Systems Research*, vol. 116, pp. 29–35, 2014.
- [11] A. Canova and B. Vusini, "Design of axial eddy-current couplers," *IEEE Transactions on Industry Applications*, vol. 39, no. 3, pp. 725–733, 2003.
- [12] A. Canova and B. Vusini, "Analytical modeling of rotating eddy-current couplers," *IEEE Transactions on Magnetics*, vol. 41, no. 1, pp. 24–35, 2005.
- [13] N. Amati, A. Tonoli, A. Canova, F. Cavalli, and M. Padovani, "Dynamic behavior of torsional eddy-current dampers: sensitivity of the design parameters," *IEEE Transactions on Magnetics*, vol. 43, no. 7, pp. 3266–3277, 2007.
- [14] A. Tonoli, "Dynamic characteristics of eddy current dampers and couplers," *Journal of Sound and Vibration*, vol. 301, no. 3-5, pp. 576–591, 2007.
- [15] T. Lubin and A. Rezzoug, "3-D analytical model for axial-flux eddy-current couplings and brakes under steady-state conditions," *IEEE Transactions on Magnetics*, vol. 51, no. 10, 2015.
- [16] T. Lubin and A. Rezzoug, "Steady-state and transient performance of axial-field eddy-current coupling," *IEEE Transactions on Industrial Electronics*, vol. 62, no. 4, pp. 2287–2296, 2015.
- [17] Y. Wang, Z. Liu, H. Yang, Z. Shao, and Z. Zhuang, "FE analysis of rock with hydraulic-mechanical coupling based on continuum damage evolution," *Mathematical Problems in Engineering*, vol. 2016, Article ID 8534965, 2016.



Hindawi

Submit your manuscripts at
<https://www.hindawi.com>

